



Microwave-assisted integration of transition metal oxide nanocoatings on manganese oxide nanoarray monoliths for low temperature CO oxidation

Junkai He^a, Sheng-Yu Chen^b, Wenxiang Tang^{a,c}, Yanliu Dang^a, Peter Kerns^b, Ran Miao^b, Biswanath Dutta^b, Pu-Xian Gao^{a,c,*}, Steven L. Suib^{a,b,c,*}

^a Institute of Materials Science, University of Connecticut, Storrs, CT, 06269-3136, United States

^b Department of Chemistry, University of Connecticut, Storrs, CT, 06269-3060, United States

^c Department of Materials Science and Engineering, University of Connecticut, Storrs, CT, 06269-3136, United States



ARTICLE INFO

Keywords:

CO oxidation
Manganese oxide
Core-shell heterostructure
Nanoarray monolithic catalysts
Microwave synthesis

ABSTRACT

Manganese oxide (OMS-2), a promising exhaust treatment catalyst, has been successfully integrated onto the channel wall surfaces of cordierite honeycombs in the form of a nanoarray forest. To further improve their catalytic carbon monoxide (CO) oxidation activity, a series of different metal oxide nanocoatings were uniformly grown on the surface of OMS-2 nanoarrays by utilizing a facile and fast microwave-assisted synthesis method. The manganese-cobalt oxide core-shell nanoarray based monolithic catalysts exhibit the highest catalytic performance with a 100% CO conversion at 150 °C, in a sharp contrast with 325 °C for the bare OMS-2 nanoarrays. Different growth mechanisms of the layered $\text{Co}(\text{OH})_2$ and spinel Co_3O_4 induced by different cobalt precursors are used to explain the morphology evolution of the manganese-cobalt oxide core-shell nanoarrays. The Co^{3+} distributed on the surface of the nanoarrays acts as the active sites for CO oxidation. The small grain size, abundant surface-adsorbed oxygen, and interfacial effects between MnO_2 and Co_3O_4 were found to favor the observed high catalytic activity. A thermal annealing study showed that high temperature induces the sintering of the nanoarray catalyst, which further affects the CO oxidation activity. This fast, cost-effective, and scalable method will provide a new route for synthesizing efficient core-shell nanoarray monolithic catalysts for low temperature catalysis.

1. Introduction

Extensive research efforts have been focused on the catalytic conversion of carbon monoxide (CO) to carbon dioxide (CO_2) in the past two decades, due to the crucial role that CO plays in various applications including proton exchange membrane fuel cells, automobile exhaust gas treatment, and CO gas sensors [1–3]. To date, platinum group metal (PGM)-based catalysts, such as platinum (Pt) [4], palladium (Pd) [5,6], and gold (Au) [7], have been widely studied due to their exceptionally high catalytic activity for CO oxidation. However, these supported noble metals are naturally scarce and prohibitive. Over the long run, using relatively cheap, earth-abundant, and highly stable transition metal alternatives, such as metal oxides, perovskites, and spinels, are being pursued as alternatives in order to achieve good CO oxidation activity at low temperature [8–10].

Different transition metal oxide based monolithic nanoarrays (ZnO , Co_3O_4 , TiO_2 , MnO_2 , and CeO_2) were invented as a new class of automotive catalytic converters to treat deteriorating environments and

ever tight regulations for emission control [11–13]. Unlike the catalysts in powder or pellet form, these unique monolithic configurations allow low catalyst loading with high surface area, good mass-transfer, and low pressure drop, and as a result, more cost effective and catalytically efficient pathways were developed. The state-of-the-art industrial catalytic converter was designed by washcoating mesoporous Al_2O_3 supported Pt/Pd on monolithic substrates with coating thicknesses of 20–200 μm . Since this method is unable to effectively control the structure of catalysts, or substrate adherence, or catalyst dispersion, washcoating is not practical for optimum utilization of catalysts. Monolithic nanoarray catalysts can reduce 10–40 times the material usage of washcoating ones without sacrificing catalytic performance [11]. In addition, the uniform distribution of vertically-aligned nanorod arrays may allow much more efficient and faster molecular diffusion and heterogeneous reactions on the surfaces.

With promising emission-control efficiency, versatile synthetic approaches have been developed to integrate nanoarrays on various substrates for the removal of pollutant emissions generated from

* Corresponding authors at: Institute of Materials Science, University of Connecticut, Storrs, CT, 06269-3136, United States.

E-mail addresses: puxian.gao@uconn.edu (P.-X. Gao), steven.suib@uconn.edu (S.L. Suib).

engines, combustors, as well as other energy devices [13,14]. Lithography processes [15] and template-assisted syntheses [16] are reported effective for large-scale fabrication of nanoarrays with precise control of the geometry, however, they are limited by relatively complicated preparation procedures. The facile and cost-effective wet chemical hydrothermal synthesis is one of the most promising bottom-up methods for large-scale fabrication of nanoarrays. Recent studies demonstrate that nanoarrays not only can be integrated on the cordierite monoliths in a short time but also are scalable with the assistance of microwave heating [17].

Coating a layer of transition metal oxide on the surface of single-metal oxide nanoarrays is considered an effective way to further enhance the catalytic performance, as the core-shell structure displayed promising catalytic properties. Many transition metal oxides reported with similar configurations showed higher CO oxidation activity than single metal oxides, such as CuO/CeO₂ [18], ZnCo₂O₄@CeO₂ [19], and MnO_x-CeO₂ [20] etc. The interface between the core and shell components could provide reaction sites for CO oxidation. The strong interaction of different components promotes synergistic effects for catalysis. Beside boosting the catalytic activity, the core-shell structure might also improve the stability and dispersibility of the materials.

Herein, we report for the first time a successful integration of ten different MnO₂/metal oxide core-shell nanoarrays onto monolithic cordierite substrates using a facile and energy-saving synthetic strategy for the catalytic oxidation of CO. To achieve the core-shell nanoarray architecture, cryptomelane type manganese oxide (OMS-2) nanoarrays were selected as the core supports to grow on the cordierite substrate first, using a facile hydrothermal synthesis as reported [21]. Since manganese is naturally abundant, multi-valent, and environmentally benign. Most importantly manganese-based oxides are widely used in industry and have shown remarkable activity for the oxidation of CO and hydrocarbons at low temperature [22–25]. Different metal oxide shells were prepared using efficient and fast microwave-assisted hydrothermal synthesis strategies, in which urea hydrolysis as a general process was applied for most metal oxides. The nanoarray materials were further annealed at 350 °C. CO oxidation performance of each core-shell nanoarray catalyst was evaluated and the trends of reactivity are given here [26]. In addition, factors such as annealing temperature and cobalt precursors for manganese-cobalt oxide core-shell nanoarrays were studied in order to probe the outstanding CO oxidation activity. Various characterization methods such as scanning electron microscopy (SEM), high-resolution transmission electron microscopy (HR-TEM), x-ray photoelectron microscopy (XPS), hydrogen-temperature programmed reduction (H₂-TPR), oxygen-temperature programmed desorption (O₂-TPD), and thermogravimetric mass spectrometry (TGA-MS) were used to examine the structure-property relations of the materials. The effects of synthesis, reducibility, surface area, and oxidation states are discussed in this work.

2. Experimental

2.1. Chemicals

All chemicals were used as received without further purification. Manganese sulfate monohydrate (MnSO₄·H₂O, ≥ 99%), nickel nitrate hexahydrate (Ni(NO₃)₂·6H₂O, ≥ 98%), zinc nitrate hexahydrate (Zn(NO₃)₂·6H₂O, ≥ 98%), cobalt nitrate hexahydrate (Co(NO₃)₂·6H₂O, ≥ 98%), cobalt acetate tetrahydrate (Co(CH₃COO)₂·4H₂O, ≥ 98%), cobalt chloride hexahydrate (CoCl₂·6H₂O, ≥ 98%), cobalt sulfate heptahydrate (CoSO₄·7H₂O, ≥ 99%), cobalt acetylacetone (Co(C₅H₇O₂)₃, 97%), potassium permanganate (KMnO₄, ≥ 99%), iron nitrate nonahydrate (Fe(NO₃)₃·9H₂O, ≥ 98%), cerium nitrate hexahydrate (Ce(NO₃)₃·6H₂O, ≥ 99%), gallium acetylacetone (Ga(C₅H₇O₂)₃, 98%), urea (CH₄N₂O, ≥ 98%), concentrated sulfuric acid (H₂SO₄, 95–98%), and concentrated hydrochloric acid (HCl, 37%) were purchased from Sigma-Aldrich. Potassium chlorate (KClO₃, ≥ 99%) was purchased

from J.T. Baker. Titanium oxide sulfate sulfuric acid hydrate (TiOSO₄·xH₂O + H₂SO₄), copper acetate (Cu(CH₃COO)₂·6H₂O, ≥ 98%), and potassium tin oxide (K₂SnO₃·3H₂O, ≥ 95%) were purchased from Alfa Aesar. The cordierite honeycomb monolith substrates were purchased from Corning Corp.

2.2. Materials synthesis

2.2.1. OMS-2 nanoarray catalysts

The cordierite substrate was washed with ethanol, water, and acetone, respectively, and dried for use. The OMS-2 nanoarray catalyst was synthesized as reported before [21]. Specifically, 13.7 g of MnSO₄·H₂O and 17.4 g of KClO₃ were dissolved in 270 mL of DDI water with 4.5 mL of H₂SO₄. The dissolved mixture was reacted at 90 °C for 12 h. After the reaction, the OMS-2 nanoarray coated cordierite substrate was washed with DDI water several times using sonication and dried in a vacuum oven overnight.

2.2.2. NiO, CuO, Fe₂O₃, ZnO, CeO₂, Ga₂O₃, and SnO₂@OMS-2 nanoarray catalysts

All these core-shell catalysts were synthesized using each metal source to react with urea. For example, OMS-2@NiO was synthesized by dissolving 0.218 g of Ni(NO₃)₂·6H₂O and 0.36 g of urea in 15 mL of DDI water and ethanol (volume ratio 1:1) mixture in a 30 mL microwave reactor vial. Then, an 8 mm × 8 mm × 10 mm (W × H × L) size OMS-2 nanoarray coated cordierite substrate was dropped into the solution and the vial was sealed. The reaction was performed in a programmable Biotage Initiator microwave reactor at 120 °C for 30 min. After the reaction, the coated substrate was washed with DDI water several times and dried in a vacuum oven overnight.

2.2.3. OMS-2@Co₃O₄ nanoarray catalysts

The synthesis procedure is the same as stated above. Five different cobalt reagents of cobalt nitrate hexahydrate (OMS-2@Co₃O₄-NO₃), cobalt acetate tetrahydrate (OMS-2@Co₃O₄-ac), cobalt chloride hexahydrate (OMS-2@Co₃O₄-Cl), cobalt sulfate heptahydrate (OMS-2@Co₃O₄-SO₄), and cobalt acetylacetone (OMS-2@Co₃O₄-acac) were used, and catalysts were named based on the anions. OMS-2@Co₃O₄ in this work stands for cobalt acetylacetone.

2.2.4. OMS-2@TiO₂ nanoarray catalyst

0.3 g of TiOSO₄·xH₂O + H₂SO₄ was dissolved in 15 mL of DDI water and ethanol (volume ratio 1:1) mixture in a 30 mL vial. Then, an 8 mm × 8 mm × 10 mm size of OMS-2 nanoarray coated cordierite substrate was drop into the solution and the vial was sealed. The vial was put into the Biotage Initiator microwave reactor and allowed to react at 120 °C for 30 min. After the reaction, the coated substrate was washed with DDI water several times and dried in a vacuum oven overnight.

2.2.5. OMS-2@MnO₂ nanoarray catalyst

0.032 g of KMnO₄ was dissolved in 15 mL of DDI water with 83 μL of concentrated HCl in a 30 mL vial. Then, an 8 mm × 8 mm × 10 mm size of OMS-2 nanoarray coated cordierite substrate was drop into the solution and the vial was sealed. The vial was put into the Biotage Initiator microwave reactor and allowed to react at 120 °C for 30 min. After the reaction, the coated substrate was washed with DDI water several times and dried in a vacuum oven overnight.

2.3. Materials characterization

A Rigaku Ultima IV diffractometer (Cu K α radiation, $\lambda = 1.5406 \text{ \AA}$) with a working voltage of 40 kV and current of 44 mA, was used for the crystal structure study of the materials. N₂ sorption analysis was performed with the aid of a Quantachrome NOVA 2000e automated sorption system. The samples were degassed at 120 °C for 6 h before

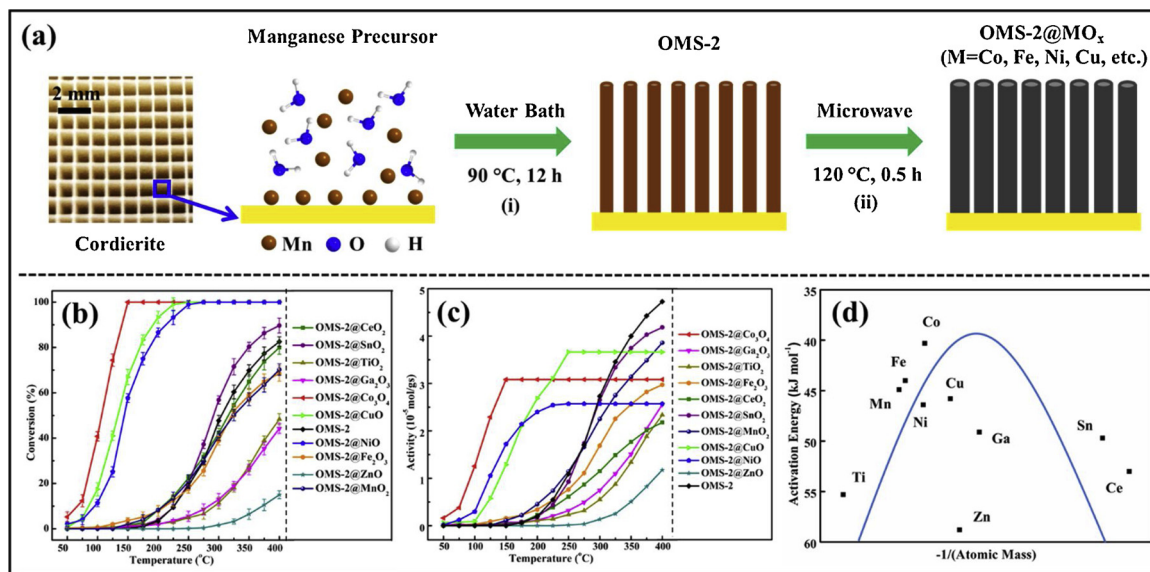


Fig. 1. (a) Schematic illustration of two-step synthesis of manganese oxide-based core-shell nanoarrays on cordierite monoliths. (b) Catalytic performance of different manganese oxide-based core-shell nanoarray catalysts for CO oxidation. (c) Calculated activities as a function of the temperature. (d) The activation energy trend of different core-shell nanoarray catalysts as a function of the atomic mass.

tests. The Brunauer-Emmett-Teller (BET) method was used for surface area calculations. The overall morphologies of the materials were observed using a FEI Nova NanoSEM 450 equipped with an energy dispersive x-ray spectroscopy (EDX) detector. The working voltage was 2.0 kV. A Talos F200X microscope operating at 200 kV coupled with an EDX detector was applied for the HR-TEM and scanning transmission electron microscopy (STEM) measurements. X-ray photoelectron spectra (XPS) of the synthesized materials were collected on a PHI model Quantum 2000 spectrometer with scanning ESCA multiprobe (Physical Electronics Industries Inc.), using Al K α radiation ($\lambda = 1486.6$ eV) as the radiation source. The spectra were recorded in the fixed analyzer transmission mode with pass energies of 187.85 eV and 29.35 eV for recording survey and high-resolution spectra, respectively. The powder samples were pressed on a double-sided carbon tape mounted on an Al coupon pinned to a sample stage with a washer and screw and then placed in the analysis chamber. Binding energies (BE) were measured for Co 2p, Mn 2p, Mn 3s and O 1s. The XPS spectra obtained were analyzed and fitted using CasaXPS software (version 2.3.16). Sample charging effects were eliminated by correcting the observed spectra with the C 1s BE value of 284.8 eV. Thermogravimetric analysis/mass spectrometry (TGA-MS) was carried out under Ar using a Netzsch Libra TG209 F1 thermogravimetric analyzer coupled to a Netzsch Aëlos QMS 403C quadrupole mass spectrometer. The temperature was ramped from room temperature to 800 °C at a rate of 10 °C min⁻¹.

H₂-TPR was carried out with an MKS gas analyzer coupled with a quadrupole mass-selective detector. 100 mg of catalyst was loaded into a quartz tube and mounted into the furnace. The samples were pretreated in argon (Ar) at 200 °C for 1 h to remove any adsorbed molecules and impurities and then cooling down to room temperature. Then a 10% H₂/Ar flow through the tube reactor at a flow rate of 50 standard cubic centimeters per minute (sccm). The temperature was ramped to 550 °C at a ramping rate of 10 °C min⁻¹. O₂-TPD was performed on a Chemisorption system (ChemiSorb 2720, Micromeritics Cor.), equipped with a U-shaped quartz reactor. About 50 mg of sample was loaded into the reactor and pretreated under 10% O₂/Ar at 300 °C for 1 h before desorption. The temperature was ramped to 750 °C at a ramping rate of 10 °C min⁻¹.

2.4. Catalytic tests

Catalytic oxidation of CO was studied for the evaluation of the

performances of all the catalysts. The CO catalytic reaction was tested in a continuous flow fixed bed quartz tubular reactor. For each test, a 5 mm × 5 mm × 10 mm size of monolith catalyst was packed in 7-mm-diameter quartz tube. Before the measurements, the catalysts were pretreated at 100 °C for 1 h under N₂ flow (100 sccm) to remove any residue adsorbed on the surface of catalysts. For CO oxidation test, the feed gas used was composed with 1% CO, 10% O₂, and balanced by N₂ with the flow rate of 100 sccm and space velocity (SV) of 24,000 h⁻¹. A gas chromatograph (GC) equipped with a molecular sieve 13X packed column and a thermal conductivity detector (SK1 8610C) was used for the online catalytic product analysis. The reaction conversion was calculated using N₂ as an internal standard. The GC peak areas of CO, O₂, N₂, and CO₂ were proportional to their concentrations. The initial peak area of CO was corrected according to Eq. (1).

$$\text{CO}_{(\text{initial})} = \frac{\text{CO}_{(\text{blank})} \times \text{N}_2(\text{sample})}{\text{N}_2(\text{blank})} \times 100\% \quad (1)$$

CO conversion was calculated using Eq. (2).

$$\text{CO conversion} = \frac{\text{CO}_{(\text{initial})} - \text{CO}_{(\text{sample})}}{\text{CO}_{(\text{initial})}} \times 100\% \quad (2)$$

3. Results

3.1. Materials characterization

The general process for the synthesis of different metal oxide core-shell nanoarrays on a cordierite substrate is shown in Fig. 1a. The single channel of the cordierite monolith is about 1 mm in diameter. In the synthesis step (i), manganese oxide nanoarrays were achieved through a slow oxidation and accumulation process using KClO₃ as oxidant in a water bath at 90 °C [21]. Heterogeneous nucleation was believed to occur on the surface of substrates forming of seed layer, followed by growing nanorods along the preferred planes to form nanoarray architectures. In step (ii), microwave-assisted hydrothermal method was used for coating of the shell in a short time to achieve an even distribution. Fig. 1b reflects the catalytic performances of different nanoarrays for CO oxidation at the SV of 24,000 h⁻¹. OMS-2@Co₃O₄ catalyst displays the best reactivity for CO oxidation, with the light-off temperature as low as around 120 °C and the full CO conversion

temperature at about 150 °C. The reactivity was followed by OMS-2@CuO and OMS-2@NiO, with full conversion temperatures at 250 °C and 275 °C, respectively, while OMS-2@ZnO nanoarrays show poor catalytic activity for CO oxidation. OMS-2 nanoarray catalyst showed moderate CO oxidation performance, even coating another layer of manganese oxide on the surface. As shown in Fig. 1c, OMS-2@Co₃O₄, OMS-2@CuO, and OMS-2@NiO showed similar shapes in their activity curves, of which OMS-2@Co₃O₄ gave the highest activity than others and achieved its maximum rate at 150 °C. To better understand the activity trend of these catalysts, a volcano plot of activation energy as a function of atomic mass was given (Fig. 1d). Of these ten selected metal oxides (mainly in period four), OMS-2@Co₃O₄ gave the lowest activation energy. The result also approves that Co₃O₄ is the state-of-the-art most active non noble metal oxide for CO oxidation, which has been extensively studied in the past decades.

The activation energy was calculated using the Arrhenius equation, $r = A \exp(-E_a/RT) [CO]^a [O_2]^b$ where r is the rate coefficient, E_a is the activation energy, A is the pre-exponential factor, R is the universal gas constant, T is the temperature in K. The CO conversion was controlled below 15% for the reaction rate calculation, as the concentrations of both CO and O₂ are approximately constant. Thus, $\ln r$ and $1/RT$ showed a linear relationship of $\ln r = -E_a/RT + \ln A$. The activation energy, pre-exponential factor, and Arrhenius plot correlation coefficients (R^2) of different transition metal oxide core-shell catalysts are summarized in Table 1. The activation energies of the manganese-metal oxide core-shell nanoarray monolith catalysts are generally consistent with the activities for CO oxidation. The pre-exponential factors of the manganese-metal oxide catalysts maintained the same order of magnitude of 10^{2-3} , of which OMS-2@Co₃O₄, OMS-2@CuO, OMS-2@NiO, and OMS-2@CeO₂ are an order of magnitude higher than other core-shell catalysts.

Optical photographs, elemental analyses, morphologies, and structures of OMS-2 nanoarrays after coating on the cordierite substrate are summarized in Fig. 2. The as-prepared OMS-2 nanoarray monolith is dark brown in color (Fig. 2a). EDX elemental mapping (Fig. 2b) for the single channel of cordierite monolith substrate demonstrates the successful coating of manganese oxide on the surface. SEM image in Fig. 2c shows a uniform distribution of OMS-2 nanoarrays on the cordierite, with the average rod length of ~4 μm (Fig. 2d). TEM images presented in Fig. 2e show smooth surfaces of OMS-2 nanorods, as well as a decreased diameter of nanorods along the crystal growing direction, which are due to the diminishing concentration of manganese reagent with coating time. The diameter of ~100 nm for the nanorods was measured in the selected area. The selected area electron diffraction (SAED) pattern shows a single crystal characteristic for the rods of OMS-2. The lattice fringes in Fig. 2f with d -spacings of 0.25 and 0.31 nm were

measured for the HR-TEM, and correspond to the (400) and (310) crystal planes of α-MnO₂.

Powder x-ray diffraction (XRD) studies were done on ten different metal oxides coated on the OMS-2 nanoarrays. The precipitates collected after each microwave-assisted hydrothermal reaction were used for the XRD characterization, due to the relative low diffraction intensities of nanoarray materials compared to the cordierite substrate, as shown in Fig. 3. In order to make the characterization consistent with the nanoarray catalysts used in CO oxidation, all the powders were washed and calcined at 350 °C. Pure crystalline phases of different metal oxides were identified for the coatings, while the corresponding crystal planes of each diffraction peak are labeled on top. The JCPDS numbers of each XRD diffraction pattern are summarized in Table 1. The morphologies of the core-shell nanoarrays vary with the metal oxides as revealed in SEM studies. Small nanoparticles were observed on the surface of OMS-2 nanorods after coating with CeO₂, Co₃O₄, CuO, TiO₂, SnO₂, and Ga₂O₃. A layered structure was found for surfaces of nanorods for the NiO coating. In addition, a unique quadrangular morphology appeared after coating with another layer of manganese oxide on nanoarrays. The chemical compositions of different metal oxide core-shell nanoarrays were determined by EDX (Table 1).

TEM was performed to better understand the morphology and configuration of nanoarrays, as presented in Fig. 4. Three different nanorods of OMS-2@Co₃O₄-NO₃ (Fig. 4a), OMS-2@Fe₂O₃ (Fig. 4b), and OMS-2@CuO (Fig. 4c) are shown. Rough surfaces composed of fine nanoparticles were observed for both OMS-2@Co₃O₄-NO₃ and OMS-2@CuO. However, it is still hard to determine the thickness of coating layers for these materials, especially for the OMS-2@Fe₂O₃ nanoarrays. The elemental mapping obtained from EDX shows that we could easily distinguish the manganese oxide core from the coating layers for different core-shell nanoarrays. As a result, a thin film of Fe₂O₃ was observed for the shell of the OMS-2@Fe₂O₃ nanoarrays. BET surface areas of the bare cordierite substrate as well as the ones that were coated with different metal oxide nanoarrays were calculated based on the results of N₂ sorption, as summarized in Table 1. The surface area was increased as high as 5–30 times for the cordierite monolith after coating with different metal oxide core-shell nanoarrays.

Knowing the performances of different metal oxide core-shell nanoarray catalysts for CO oxidation, we further studied the cobalt oxide coated nanoarrays synthesized with different cobalt precursors, in the hopes of better understanding the structure and property relationship of the material, and as a result, were able to design catalysts with high activity at low temperature. CO oxidation behavior of each catalyst varied with the cobalt reagents used in the synthesis. As shown in Fig. 5a, OMS-2@Co₃O₄-acac displayed the best performance for complete conversion of CO at a low temperature of 150 °C, followed by

Table 1
Summary of Chemical Composition, BET Surface Area, and Catalysis Parameters of Catalysts.

catalyst	JCPDS number	mass loading (%)	metal/Mn ratio by EDX	surface area (m ² g ⁻¹)	T ₅₀ (°C)	E _a (kJ mol ⁻¹)	A (mol g ⁻¹ s ⁻¹)	R ²
OMS-2@Co ₃ O ₄ -acac	42-1467	23	1.88	17	110	40.3	1.6×10^3	0.994
OMS-2@Co ₃ O ₄ -ac	42-1467	16	1.42	28	115	52.8	2.8×10^4	0.998
OMS-2@Co ₃ O ₄ -NO ₃	42-1467	20	0.41	16	125	49.8	6.7×10^3	0.998
OMS-2@Co ₃ O ₄ -Cl	42-1467	12	0.4	19	165	37.7	4.2×10^2	0.992
OMS-2@Co ₃ O ₄ -SO ₄	42-1467	10	0.37	20	200	27.7	0.9×10^1	0.997
OMS-2@CuO	48-1548	16	0.55	14	140	45.8	1.7×10^3	0.995
OMS-2@NiO	47-1049	19	1.05	20	150	46.4	4.7×10^3	0.998
OMS-2@Fe ₂ O ₃	–	13	0.11	14	325	44	0.7×10^2	0.999
OMS-2@CeO ₂	34-0394	18	4.04	24	325	53	1.5×10^3	0.998
OMS-2@TiO ₂	73-1764	9	0.15	28	400	55.3	8.2×10^2	0.999
OMS-2@Ga ₂ O ₃	06-0503	10	0.22	5	425	49.1	2.9×10^2	0.999
OMS-2@SnO ₂	21-1250	12	0.19	7	300	49.7	6.5×10^2	0.994
OMS-2@ZnO	05-0664	8	0.69	14	–	58.8	4.4×10^2	0.995
OMS-2@MnO ₂	29-1020	10	–	32	325	44.9	3.9×10^2	0.998
OMS-2	29-1020	6	–	25	325	43.9	1.4×10^2	0.993
cordierite	12-0303	–	–	1	–	–	–	–

The “–” stands for not applicable or measured.

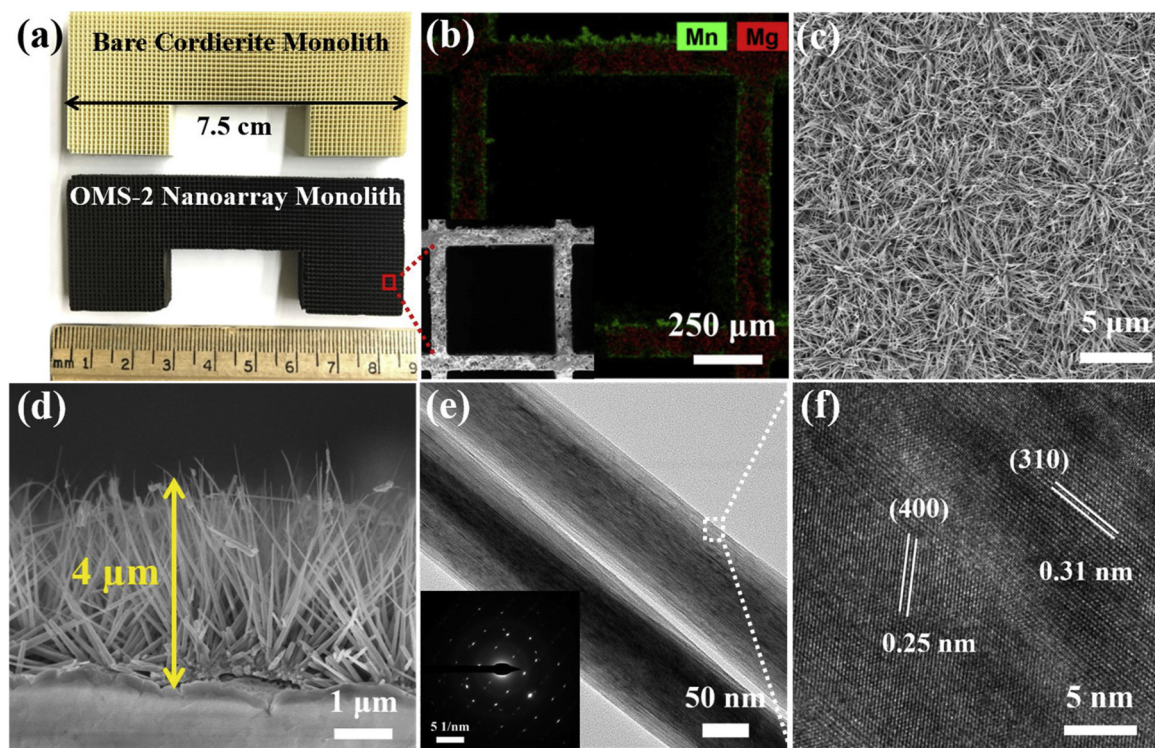


Fig. 2. (a) Photograph of OMS-2 coated nanoarray monoliths. (b) EDX mapping of single channel of OMS-2 coated cordierite substrate, inset for the cross-section view. SEM images (c) top view and (d) cross section view of OMS-2 nanoarrays. (e) TEM image of the OMS-2 nanorods. Inset for the SAED pattern of the rod. (f) HR-TEM image of OMS-2 nanorod.

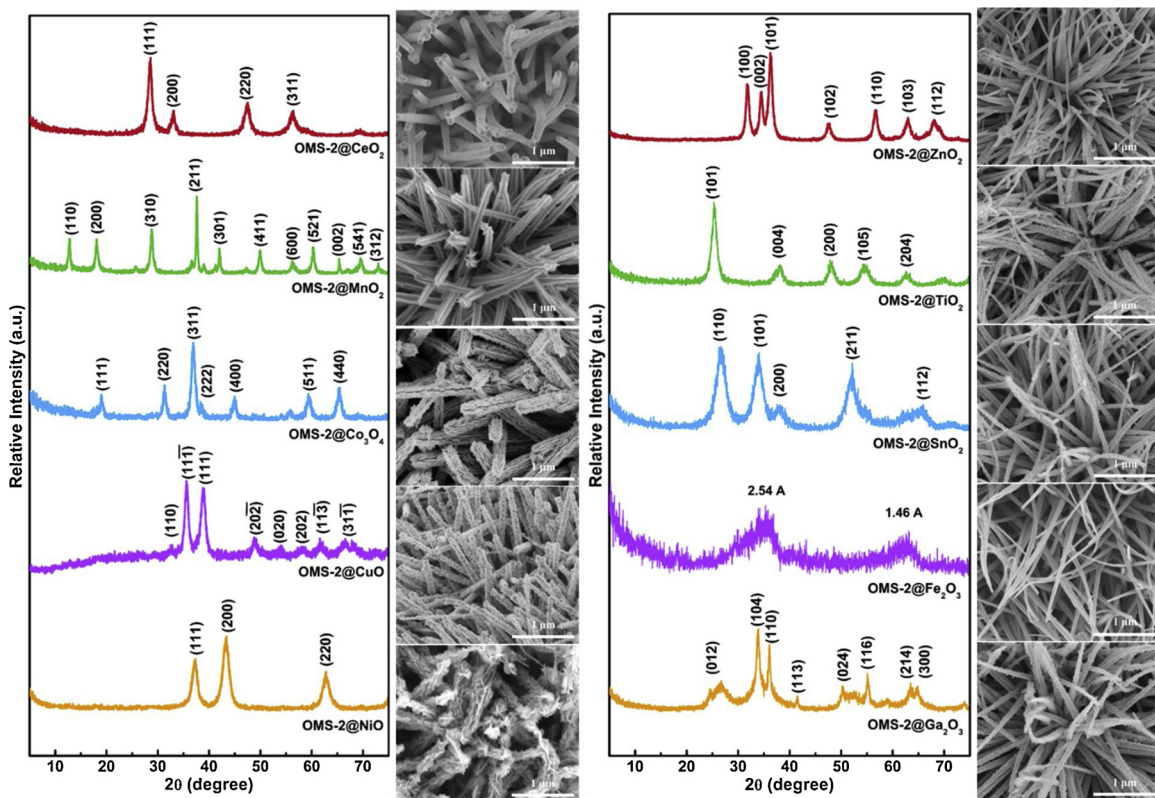


Fig. 3. XRD patterns of ten different metal oxides and correspond SEM images for core-shell nanoarrays.

OMS-2@Co₃O₄-ac and OMS-2@Co₃O₄-NO₃ at a temperature of 175 °C. Compared to the catalysts above, OMS-2@Co₃O₄-Cl and OMS-2@Co₃O₄-SO₄ need temperatures as high as 225 °C and 300 °C,

respectively, to achieve 100% conversion (T_{100}). The changes of mass loadings and surface areas of different manganese-cobalt oxide nanoarrays on the cordierite monoliths were induced by the precipitation

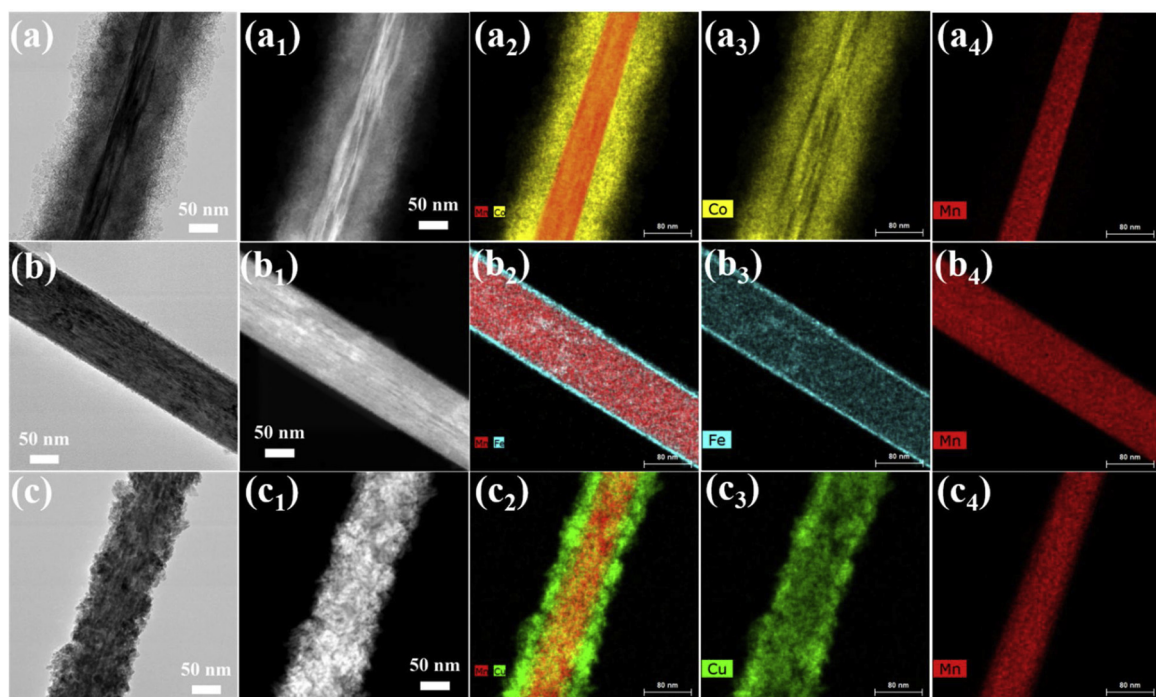


Fig. 4. Representative TEM, STEM, and EDX mapping images of (a) OMS-2@ Co_3O_4 - NO_3 , (b) OMS-2@ Fe_2O_3 , and (c) OMS-2@ CuO core-shell nanoarrays.

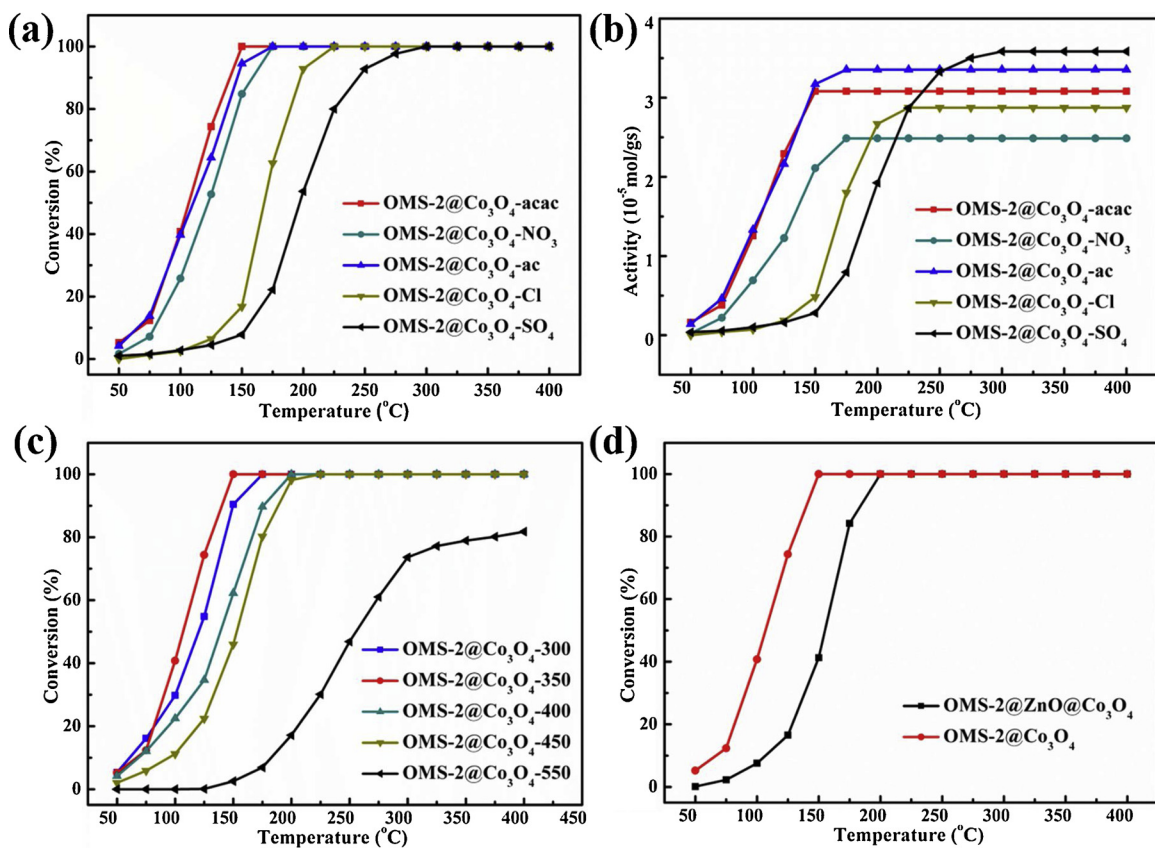


Fig. 5. (a) Catalytic performance of different manganese-cobalt oxide core-shell nanoarray catalysts for CO oxidation. (b) Calculated activities as a function of the temperature. (c) Catalytic performance of OMS-2@ Co_3O_4 -acac core-shell nanoarray catalysts for CO oxidation at different activation temperatures. (d) CO oxidation reactivities of OMS-2@ Co_3O_4 and OMS-2@ ZnO @ Co_3O_4 monolith catalysts.

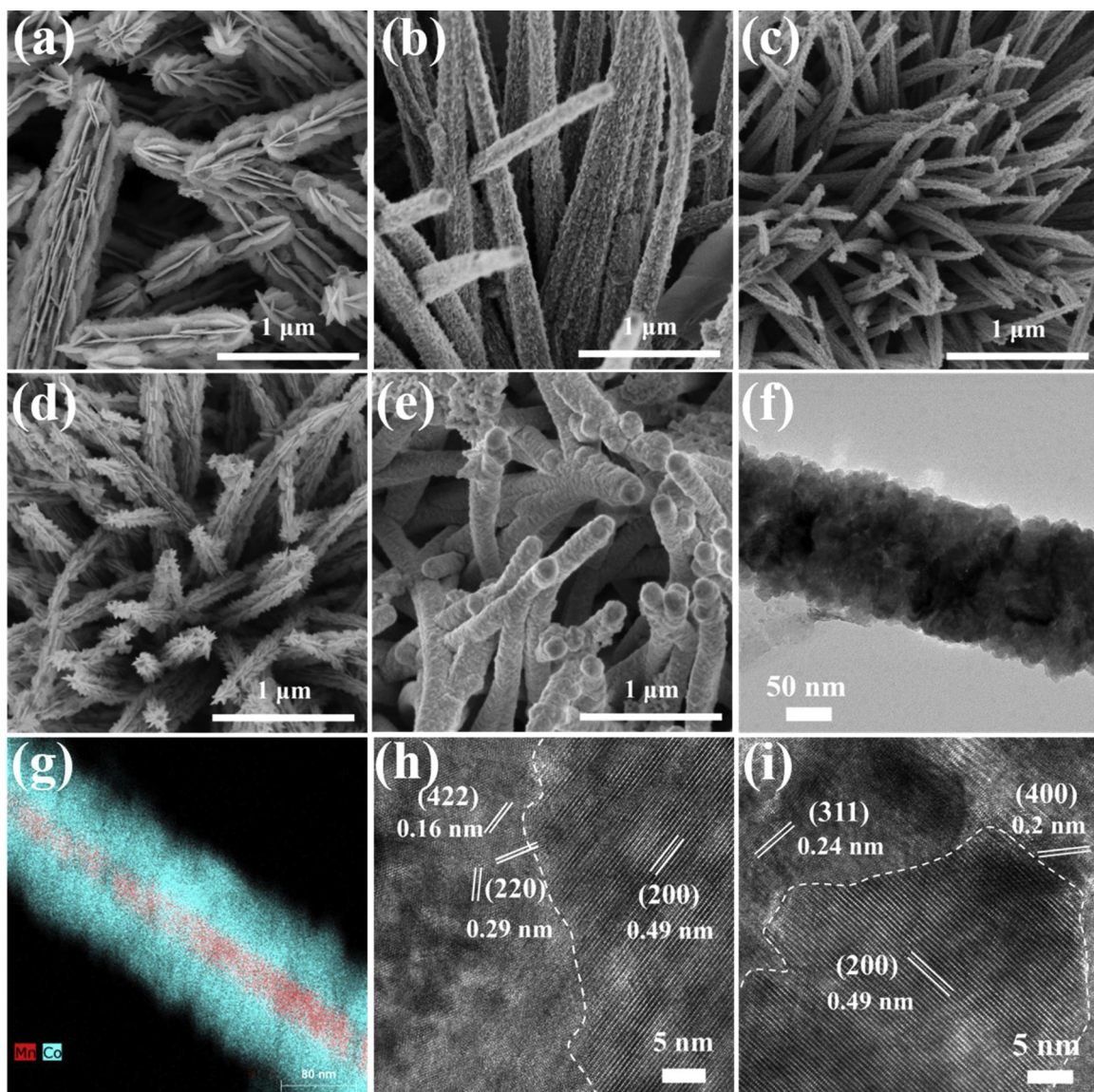


Fig. 6. SEM images of (a) OMS-2@ Co_3O_4 - NO_3 , (b) OMS-2@ Co_3O_4 -ac, (c) OMS-2@ Co_3O_4 - SO_4 , (d) OMS-2@ Co_3O_4 -Cl, and (e) OMS-2@ Co_3O_4 -acac. (f) TEM and (g) EDX mapping images of OMS-2@ Co_3O_4 -acac nanoarrays. HR-TEM images of OMS-2@ Co_3O_4 -acac after calcination at (h) 350 °C and (i) 550 °C.

rates of Co precursors. The reactivity of the monolithic catalysts was compared by calculating the activities after normalization with the loading weight. As presented in Fig. 5b, the normalized activity of the catalysts follows the trend of OMS-2@ Co_3O_4 -acac \approx OMS-2@ Co_3O_4 -ac $>$ OMS-2@ Co_3O_4 - NO_3 $>$ OMS-2@ Co_3O_4 -Cl $>$ OMS-2@ Co_3O_4 - SO_4 . In addition, activation temperatures were also studied for CO oxidation, using the best catalyst, OMS-2@ Co_3O_4 -acac, as shown (Fig. 5c). The catalyst showed the best CO oxidation performance at 350 °C, and higher temperature may cause catalyst sintering. The interface effect between MnO_2 and Co_3O_4 was studied by coating a thin layer of ZnO between OMS-2 nanorods and the Co_3O_4 layer. As a result, OMS-2@ZnO@ Co_3O_4 monolith catalyst displayed a decreased full conversion temperature of CO, as shown in Fig. 5d.

In order to understand the changes of activity, both SEM and HR-TEM were utilized to probe the morphological and structural differences of five manganese-cobalt oxide monolith catalysts at different calcination temperatures. Fig. 6a shows the thin flakes of Co_3O_4 perpendicularly grown on OMS-2 nanoarrays that form cactus-like morphologies, which use cobalt nitrate as the reagent. Similar morphologies were also observed for OMS-2@ Co_3O_4 -ac (Fig. 6b), OMS-2@ Co_3O_4 - SO_4 (Fig. 6c), and OMS-2@ Co_3O_4 -Cl (Fig. 6d). OMS-

2@ Co_3O_4 -acac in Fig. 6e showed successful growth of small nanoparticles on the surface of OMS-2 nanorods. The TEM images of single nanorod for OMS-2@ Co_3O_4 -acac in Fig. 6f reveal the uniform coating of Co_3O_4 nanoparticles, and EDX elemental mapping (Fig. 6g) shows a core-shell structure with the Co_3O_4 coating thickness of about 50 nm. HR-TEM images of OMS-2@ Co_3O_4 -acac after calcination at 350 and 550 °C are displayed in Fig. 6h and i, respectively. The clear lattice fringes with the measured *d*-spacing of about 0.49 nm can be indexed to the (200) planes of $\alpha\text{-MnO}_2$, suggesting that the crystalline nanorods grew along the *c* axis. [27] Crystal interfaces between Co_3O_4 and MnO_2 are observed for the core-shell nanoarrays as highlighted with the dashed line. Two types of lattice fringes were observed for the material calcined at 350 °C, and indexed to the (422) and (220) planes of Co_3O_4 . Both (311) and (400) planes were confirmed for Co_3O_4 after calcining the materials at 550 °C.

The cobalt oxide coated nanoarrays were further studied by XPS to investigate the chemical oxidation states and surface properties of catalysts, which play a vital role for the oxidation of CO. Deconvoluted spectra of Mn 2p, Mn 3s, Co 2p, and O 1s are presented in Fig. 7. Six peaks were fitted for Mn 2p_{3/2} (Fig. 7a) based on the multiplet fittings used by Biesinger et al. [28]. The full width at half maximum (FWHM)

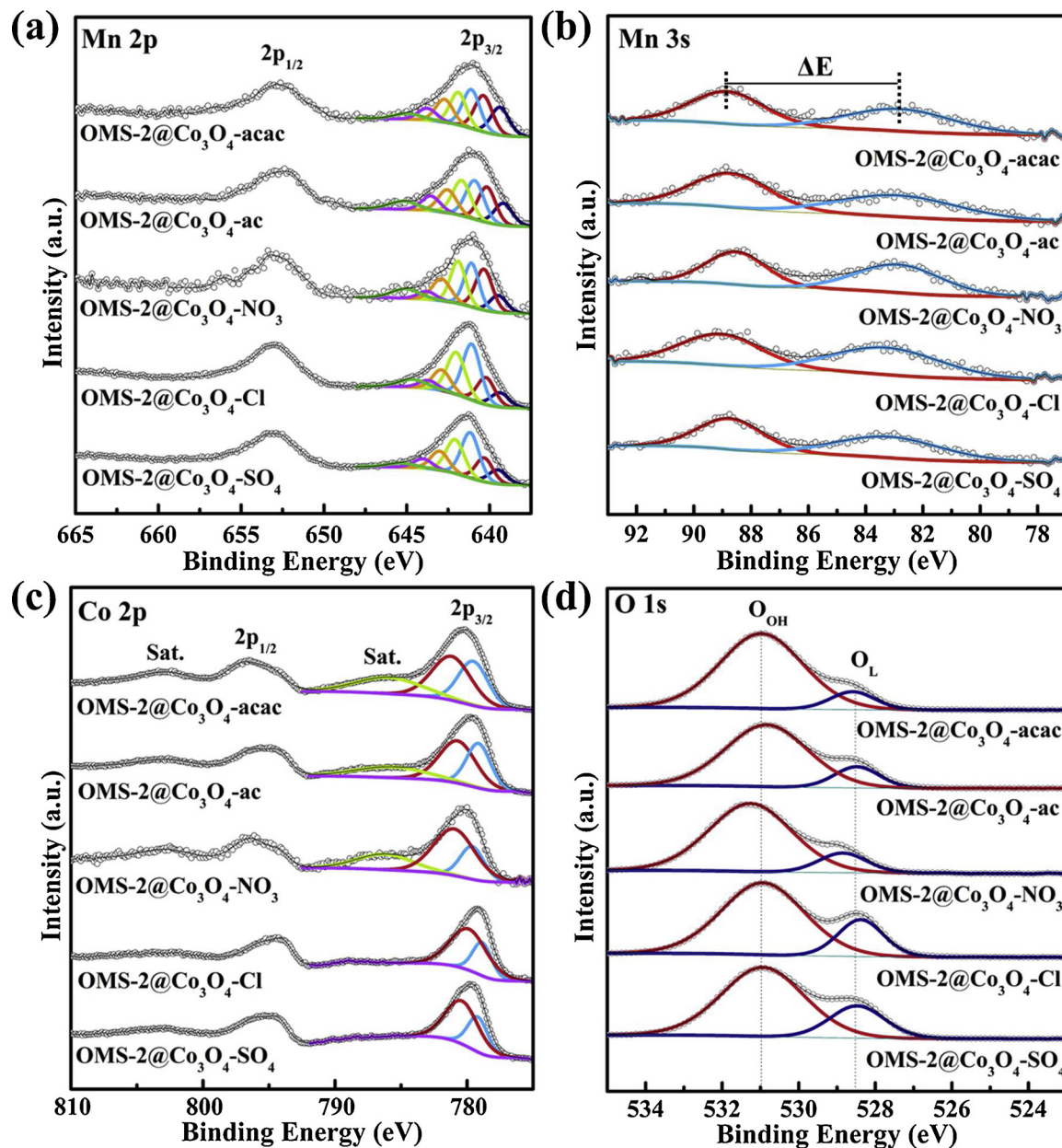


Fig. 7. Mn 2p (a), Mn 3s (b), Co 2p (c), and O 1s (d) deconvoluted XPS spectra of five different manganese-cobalt oxide core-shell catalysts. Raw data are shown by circles, and the fitted data are shown as solid lines. All the spectra were calibrated using the C 1s transition.

of each peak was constrained according to the standards reported [29]. The fitting results in Table 2 show large peak ratios at $\approx 640.4 \pm 0.2$ eV for OMS-2@Co₃O₄-acac and OMS-2@Co₃O₄-ac, indicate an oxidation state of Mn close to 2 +. The fittings for other three catalysts suggest a higher Mn oxidation state close to 3 +. We further fit the Mn 3s (Fig. 7b) to estimate the average oxidation state (AOS) of Mn, using the equation $\text{AOS} = 8.956 - 1.126 \Delta E$, where ΔE is the

binding energy difference between the multiplet splitting of Mn 3s [30]. The calculated AOS of Mn (Table 3) for different manganese-cobalt oxide catalysts demonstrates the reduction of surface OMS-2 nanorods due to the coatings of cobalt oxides. The XRD patterns of manganese-cobalt oxide films (Fig. S3) further confirmed the α -MnO₂ crystal structure of the bulk manganese oxide cores. As shown in Fig. 7c, two peaks at around 780 and 795 eV for Co 2p demonstrate the

Table 2
Summary of Fitting Parameters for Mn 2p_{3/2} Spectra.

catalyst	P1 (eV)	%	P2 (eV)	%	P3 (eV)	%	P4 (eV)	%	P5 (eV)	%	P6 (eV)	%	P7 (eV) ^a	%
OMS-2@Co ₃ O ₄ -acac	639.4	16	640.4	21	641.1	21	641.9	17	642.7	13	643.8	7	644.9	5
OMS-2@Co ₃ O ₄ -ac	639.2	12	640.2	19	640.9	22	641.7	19	642.5	13	643.5	8	645.2	7
OMS-2@Co ₃ O ₄ -NO ₃	639.5	9	640.3	23	641.1	21	641.9	21	642.9	13	643.8	5	645.1	8
OMS-2@Co ₃ O ₄ -Cl	639.4	8	640.2	15	641.1	31	642.0	24	642.9	11	643.7	4	644.7	7
OMS-2@Co ₃ O ₄ -SO ₄	639.5	9	640.3	15	641.2	30	642.1	23	643.0	13	644.0	6	645.3	4

^a P7 is a shake-up peak with FWHM of 2 eV.

Table 3Summary of Mn 3 s, Co 2p_{3/2}, and O 1s for Different Manganese-Cobalt Oxide Catalysts.

catalyst	ΔE 3 s (eV)	AOS	Co 2p _{3/2}				O 1s			
			Co ²⁺	%	Co ³⁺	%	O _L	%	O _{OH}	%
OMS-2@Co ₃ O ₄ -acac	6.02	2.2	781.2	57.1	779.5	42.9	528.6	11.5	531.0	88.5
OMS-2@Co ₃ O ₄ -ac	5.86	2.4	780.7	58.6	779.1	41.4	528.5	15.8	530.8	84.2
OMS-2@Co ₃ O ₄ -NO ₃	5.67	2.6	781.4	71.1	779.9	28.9	528.9	14.5	531.3	85.5
OMS-2@Co ₃ O ₄ -Cl	5.76	2.5	779.9	70.6	778.9	29.4	528.4	21.9	530.9	78.1
OMS-2@Co ₃ O ₄ -SO ₄	5.54	2.7	780.4	66.5	779.2	33.5	528.5	33.7	530.9	76.3

presence of Co₃O₄ [31]. The peak ratios of Co³⁺ deconvoluted from Co 2p_{3/2} are very close for OMS-2@Co₃O₄-acac and OMS-2@Co₃O₄-ac, but much higher than others, indicating that abundant Co³⁺ species exist in the catalysts. Two oxygen species were identified from the O 1s spectrum (Fig. 7d) at around 528.5 and 531 eV, corresponding to lattice oxygen (O_L) and surface hydroxyl groups (O_{OH}), respectively. The O_{OH}/O_L ratios of five catalysts follow the trend of OMS-2@Co₃O₄-acac (7.7) > OMS-2@Co₃O₄-NO₃ (5.9) > OMS-2@Co₃O₄-ac (5.3) > OMS-2@Co₃O₄-Cl (3.6) > OMS-2@Co₃O₄-SO₄ (2.3), consistent with the order of normalized activities as stated above.

The TGA curve of cordierite substrate (Fig. S4) shows less than 1 wt % loss mainly at 450–800 °C, indicating a stable structure for the high temperature reaction. The weight losses of five manganese-cobalt oxide nanoarrays at the temperature of 200–600 °C follow the trend of OMS-2@Co₃O₄-acac > OMS-2@Co₃O₄-ac > OMS-2@Co₃O₄-NO₃ > OMS-2@Co₃O₄-SO₄ > OMS-2@Co₃O₄-Cl, which mainly are due to the loss of surface oxygen species. The mass spectrum recorded for OMS-2@Co₃O₄-acac confirmed the formation of CO₂ for the weight loss due to the removal of adsorbed -acac ligands.

Reducibility of the five manganese-cobalt oxide core-shell nanoarray catalysts was measured by H₂-TPR, which was used to understand the reactivity for CO oxidation, as shown in Fig. 8a. There are generally two reduction steps for manganese oxide and cobalt oxide, respectively, including MnO₂ → Mn₃O₄ → MnO and Co₃O₄ → CoO → Co [23,24]. Higher temperature is needed for each further reduction step. The reduction reaction takes place at 200–350 °C and is assigned to the reductions of Co³⁺ to Co²⁺ (Co₃O₄ → CoO) and Mn⁴⁺ to Mn³⁺ (MnO₂ → Mn₂O₃), while the temperature ranges from 350 °C to 500 °C can be attributed to the reductions of Co²⁺ to Co⁰ (CoO → Co) and Mn³⁺ to Mn²⁺ (Mn₂O₃ → Mn₃O₄). Among those five tested materials, OMS-2@Co₃O₄-acac displayed the lowest consumption peak at around 270 °C mainly due to the reduction of Co³⁺ to Co²⁺, indicating the increased reducibility of the catalyst. In addition, O₂-TPD was performed to study the desorption behavior of oxygen species from the core-shell catalysts. As shown in Fig. 8b, the oxygen consumption peak below 275 °C can be assigned to the evolution of surface adsorbed oxygen species. The oxygen peaks ranging from 275 °C to 550 °C and above are attributed to the evolution of lattice oxygens from the near surface as well as the bulk, respectively. OMS-2@Co₃O₄-acac displayed

a distinct oxygen consumption peak at temperatures of 275–550 °C, indicating that abundant oxygen species exist on the surface. This result is consistent with the observations from XPS as stated above.

OMS-2@Co₃O₄-acac nanoarray-based monoliths as the best CO oxidation catalysts were selected for mechanical stability tests. The catalyst was sonicated in water using a Fisher Scientific Ultrasonic Cleaner with a frequency of 40 kHz. As shown in Fig. S5, the nanoarray-based monolithic catalyst maintained 90 wt% of coating after 10 h sonication and the CO oxidation characterization showed a good catalytic performance with the full CO conversion temperature of about 175 °C.

4. Discussion

Multiple oxidation states of manganese (Mn²⁺, Mn³⁺, and Mn⁴⁺) as well as the unique 2 × 2 tunnel structure are composed of edge- or corner-shared [MnO₆] octahedral units, making OMS-2 one of the most studied materials for heterogeneous catalysis [32]. OMS-2 nanoarrays reported by Chen et al. [33] showed a robust mechanical stability, and better CO oxidation performances than the classic washcoating counterparts. For the first time, different non-noble-metal oxides for CO oxidation were achieved using the fast and facile microwave method. As a result, the CO oxidation behavior of different core-shell metal oxide nanoarrays varies considerably, while metal-oxygen bond energies, CO adsorption ability, lattice oxygen mobility, and CO₂ desorption ability were considered to play crucial roles [34]. The CO reactivity of different core-shell nanoarrays was also confirmed by kinetic studies, of which OMS-2@Co₃O₄ showed a lower activation energy of 40.3 kJ mol⁻¹, demonstrating that less energy was required to break the metal-oxygen bonds. In addition, the pre-exponential factor reflects the number of active sites generated on the surfaces of catalysts [35]. The calculated pre-exponential factors of OMS-2@Co₃O₄, OMS-2@CuO, and OMS-2@NiO are several to dozens of times higher than other core-shell catalysts, together with their lower conversion temperatures, suggesting an increased number of active sites created by those coatings. In terms of practical applications, for example, the core-shell OMS-2@Co₃O₄ monolithic catalyst with less amount of cobalt, decreases the cost of materials, but achieves similar or higher CO oxidation performance compared to the direct use of Co₃O₄ nanoarrays.

The microwave-assisted hydrothermal method is the key to

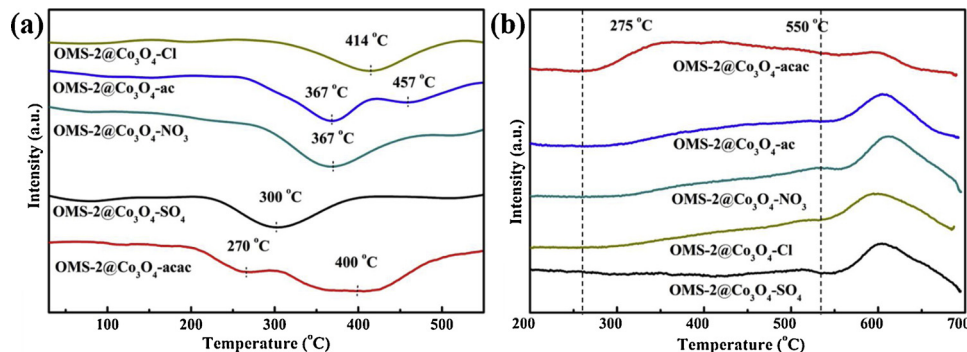


Fig. 8. (a) H₂-TPR and (b) O₂-TPD profiles of five different manganese-cobalt oxide core-shell catalysts.

achieving uniform and thin coatings for the external shell part of the nanoarray monolith [36]. Since homogenous heating caused by microwave radiation will provide uniform nucleation and growth environments for metal oxide nanoclusters, small sized Co_3O_4 nanomaterials were well dispersed on the surfaces of OMS-2 nanoarrays [37]. For comparison, we also made Co_3O_4 coatings using cobalt nitrate as a precursor utilizing the conventional hydrothermal synthesis strategy. As shown in Fig. S6, OMS-2 nanoarrays were partially coated with Co_3O_4 nanosheets after the hydrothermal reaction, which may be due to the limited cobalt precursor inside the channels of honeycomb monoliths caused by the static hydrothermal reaction environment.

Interfaces were not only found to exist in the metal-oxide, but also play an important role for the catalytic reaction in oxide-oxide systems [38,39]. Tang et al. [40] reported that heterogeneous interfaces due to the $\text{MnO}_2\text{-Co}_3\text{O}_4$ composite lowered the reduction temperature and increased the population of adsorbed oxygen species, and as a result, enhanced its catalytic activity. Similar results were observed with other metal oxides such as $\text{MnO}_2\text{@NiO}$ [41] and $\text{CeO}_2\text{@MnO}_2$ [42]. In this work, the interface effect between MnO_2 and Co_3O_4 was investigated for the best CO oxidation catalyst of OMS-2@ $\text{Co}_3\text{O}_4\text{-acac}$ core-shell nanoarrays. Based on the CO oxidation results presented above (Fig. 1b), OMS-2@ZnO catalyst exhibits much lower activity than OMS-2 nanoarrays, demonstrating the successful coating of ZnO thin layers on the surface of OMS-2 nanorods, which were selected as the active support. By applying the same synthesis method as OMS-2@ $\text{Co}_3\text{O}_4\text{-acac}$, another layer of Co_3O_4 was coated on the surface of OMS-2@ZnO nanorods, forming the OMS-2@ $\text{ZnO}\text{@Co}_3\text{O}_4$ core-shell-shell structure. The catalytic results for OMS-2@ $\text{ZnO}\text{@Co}_3\text{O}_4$ (Fig. 5d) needed a higher temperature for 100% conversion of CO when the ZnO layer exists between MnO_2 and Co_3O_4 , demonstrating that an interaction effect exists in OMS-2@ $\text{Co}_3\text{O}_4\text{-acac}$ leading to high performance in CO oxidation.

An abundant amounts of Co^{3+} exposed on the surfaces of nanoarrays were found to contribute to the high activity of CO oxidation. Actually, many papers reported that Co^{3+} is the dominant active site for CO oxidation in Co_3O_4 . For example, Xie et al. [43] prepared Co_3O_4 with controlled morphology of nanorods that have a predominant exposure of (110) planes, which are mainly composed of Co^{3+} cations, which exhibit much higher activity for CO oxidation than conventional nanoparticles. Broqvist et al. [44] revealed the CO oxidation mechanism on (110) surfaces of Co_3O_4 utilizing first principle density functional theory (DFT) and that CO prefers to adsorb on the surface of Co^{3+} sites. In this study, XPS results of OMS-2@ $\text{Co}_3\text{O}_4\text{-acac}$ displayed a higher ratio of Co^{3+} on the surface than other manganese-cobalt oxide core-shell nanoarrays, which in turn present better performance for CO oxidation. Meanwhile, the $\text{H}_2\text{-TPR}$ profile of OMS-2@ $\text{Co}_3\text{O}_4\text{-acac}$ (Fig. 8a) showed a distinct consumption peak at a lower temperature of 270 °C for $\text{Co}^{3+} \rightarrow \text{Co}^{2+}$, also indicating higher amounts of Co^{3+} distributed on the surface of the nanocrystals. These findings are consistent with the results that are reported in the literature as stated above.

As stated above, the abundant amounts of Co^{3+} exposed on surfaces and large amounts of adsorbed oxygen species stem from the interface together contribute to the high CO oxidation activity. To better understand how these work cooperatively to accomplish the catalytic cycle, three plausible reaction mechanisms are proposed for CO oxidation over manganese-cobalt oxide core-shell nanoarray catalysts, as shown in Fig. S7. Previous *in situ* diffuse reflectance infrared spectroscopy (DRIFTS) experiments conducted by Luo et al. [45] demonstrated that CO adsorbed on the surface of transition metal oxides in the forms of bidentate carbonate or carbonyl species. In this study, CO may adsorb on the surface Co metal adjacent to the interface (schematic a), or on the manganese oxide surface nearest to the interface (schematic b), or on both manganese oxide surfaces nearest to the interface and on the Co metal surface next-nearest to the interface (schematic c). For all those reaction pathways, the shared oxygens at the interface of metal

oxides are actively involved in the catalytic reaction, which was also confirmed by Shapovalov et al. [46] using DFT calculations.

In general, the CO oxidation reaction rate is determined by the step of $\text{CO}^*(\text{g}) + \text{O}_{\text{latt}} \rightarrow \text{CO}_2(\text{g}) + \text{O}_{\text{vac}}$, where O_{latt} stand for the lattice oxygen and O_{vac} for oxygen vacancies. In this process, active oxygen needs to react with the adsorbed CO for the generation of CO_2 on the surface, which requires the catalyst to have a low M-O bond energy. As a result, Co_3O_4 is one of the candidates. In addition, the high ratio of O_{OH} obtained from XPS results of O 1s (Fig. 7d), the large amount weight loss recorded by TGA (Fig. S4), as well as the clear desorption peak observed from 275 to 550 °C for the $\text{O}_2\text{-TPD}$ profile (Fig. 8b), suggest there are higher surface adsorbed oxygen species of OMS-2@ $\text{Co}_3\text{O}_4\text{-acac}$ than on other manganese-cobalt oxide core-shell nanoarrays. According to the literature [47], these adsorbed $-\text{OH}$ groups are weakly bonded on the surface, which can either directly couple with the adsorbed CO or via $-\text{COOH}$ to form CO_2 . The protons generated from the reactant site were transferred to bond with $-\text{OH}$ nearby to form adsorbed H_2O . Such $-\text{OH}$ mediated reaction would also promote the CO oxidation activity of OMS-2@ $\text{Co}_3\text{O}_4\text{-acac}$ nanoarrays. High oxygen mobility is also required for the catalyst toward efficient CO oxidation. The $\text{H}_2\text{-TPR}$ profile in Fig. 8a exhibits increased reducibility for OMS-2@ $\text{Co}_3\text{O}_4\text{-acac}$, indicating the enhanced oxygen mobility on the basis of the literature [48].

5. Conclusions

In summary, a facile and fast microwave-assisted synthetic strategy has been developed to integrate different manganese oxide nanoarray based core-shell nanostructures onto cordierite honeycomb monoliths. OMS-2@ $\text{Co}_3\text{O}_4\text{-acac}$ monolith catalyst with the 100% CO oxidation conversion temperature of 150 °C and corresponding activation energy of 40.3 kJ mol⁻¹, showed the highest CO oxidation activity among all the tested catalysts. The activity order of these catalysts is found to be closely correlated with the amount of Co^{3+} exposed on the surface, adsorbed oxygen species, and oxygen mobilities. In addition, the synergistic effect between Co_3O_4 and MnO_2 was demonstrated to play an important role for the enhanced catalytic activity. High thermal annealing temperatures induce the sintering of the core-shell nanoarrays, which further affect the CO catalytic activity. The unique microwave-assisted hydrothermal synthesis with controllable reaction rate and uniform coating exhibits good potential for the preparation of monolithic catalysts for emission control.

Acknowledgements

This work is supported by the National Science Foundation (Award No. CBET 1344792). The TEM studies were performed using the facilities in the UConn-Thermo Fisher Scientific Center for Advanced Microscopy and Materials Analysis (CAMMA). The authors would like to thank Terry Ng for the help with several experiments.

Appendix A. Supplementary data

Supplementary material related to this article can be found, in the online version, at doi:<https://doi.org/10.1016/j.apcatb.2019.117766>.

References

- [1] S. Lee, S. Mukerjee, E. Ticianelli, J. McBreen, Electrocatalysis of CO tolerance in hydrogen oxidation reaction in PEM fuel cells, *Electrochim. Acta* 44 (1999) 3283–3293.
- [2] H. Yamaura, K. Moriya, N. Miura, N. Yamazoe, Mechanism of sensitivity promotion in CO sensor using indium oxide and cobalt oxide, *Sens. Actuators B Chem.* 65 (2000) 39–41.
- [3] Z. Ren, V. Botu, S. Wang, Y. Meng, W. Song, Y. Guo, R. Ramprasad, S.L. Suib, P.X. Gao, Monolithically integrated spinel $\text{M}_x\text{Co}_{3-x}\text{O}_4$ ($\text{M}=\text{Co, Ni, Zn}$) nanoarray catalysts: scalable synthesis and cation manipulation for tunable low-temperature CH_4 and CO oxidation, *Angew. Chem. Int. Ed.* 53 (2014) 7223–7227.

[4] F. Morfin, T.S. Nguyen, J.L. Rousset, L. Piccolo, Synergy between hydrogen and ceria in Pt-catalyzed CO oxidation: an investigation on Pt–CeO₂ catalysts synthesized by solution combustion, *Appl. Catal. B Environ.* 197 (2016) 2–13.

[5] V. Bratan, C. Munteanu, C. Horoiu, A. Vasile, F. Papa, R. State, S. Preda, D. Culita, N.I. Ionescu, CO oxidation over Pd supported catalysts —In situ study of the electric and catalytic properties, *Appl. Catal. B Environ.* 207 (2017) 166–173.

[6] G. Spezzati, A. Benavidez, A.T. DeLaRiva, Y. Su, J.P. Hofmann, S. Asahina, E.J. Olivier, J.H. Neethling, J.T. Miller, A.K. Datye, E.J.M. Hensen, CO oxidation by Pd supported on CeO₂(100) and CeO₂(111) facets, *Appl. Catal. B Environ.* 243 (2019) 36–46.

[7] Y.H. Chen, C.Y. Mou, B.Z. Wan, Ultrasmall gold nanoparticles confined in zeolite Y: preparation and activity in CO oxidation, *Appl. Catal. B Environ.* 218 (2017) 506–514.

[8] P. Ciambelli, S. Cimino, S. De Rossi, L. Lisi, G. Minelli, P. Porta, G. Russo, AFEO₃ (A=La, Nd, Sm) and LaFe_{1-x}Mg_xO₃ perovskites as methane combustion and CO oxidation catalysts: structural, redox and catalytic properties, *Appl. Catal. B Environ.* 29 (2001) 239–250.

[9] C.-J. Jia, M. Schwickardi, C. Weidenthaler, W. Schmidt, S. Korhonen, B.M. Weckhuysen, F. Schüth, Co₃O₄–SiO₂ nanocomposite: a very active catalyst for CO oxidation with unusual catalytic behavior, *J. Am. Chem. Soc.* 133 (2011) 11279–11288.

[10] L. Pahalagedara, D.A. Kriz, N. Wasalathanthri, C. Weerakkody, Y. Meng, S. Dissanayake, M. Pahalagedara, Z. Luo, S.L. Suib, P. Nandi, R.J. Meyer, Benchmarking of manganese oxide materials with CO oxidation as catalysts for low temperature selective oxidation, *Appl. Catal. B Environ.* 204 (2017) 411–420.

[11] Y. Guo, Z. Ren, W. Xiao, C. Liu, H. Sharma, H. Gao, A. Mhadeshwar, P.X. Gao, Robust 3-D configurated metal oxide nano-array based monolithic catalysts with ultrahigh materials usage efficiency and catalytic performance tunability, *Nano Energy* 2 (2013) 873–881.

[12] S. Wang, Z. Ren, W. Song, Y. Guo, M. Zhang, S.L. Suib, P.X. Gao, ZnO/perovskite core-shell nanorod array based monolithic catalysts with enhanced propane oxidation and material utilization efficiency at low temperature, *Catal. Today* 258 (2015) 549–555.

[13] S. Wang, Z. Ren, Y. Guo, P.X. Gao, Nano-array integrated monolithic devices: toward rational materials design and multi-functional performance by scalable nanostructures assembly, *CrystEngComm* 18 (2016) 2980–2993.

[14] G. Centi, P. Ciambelli, S. Perathoner, P. Russo, Environmental catalysis: trends and outlook, *Catal. Today* 75 (2002) 3–15.

[15] A.R. Madaria, M. Yao, C. Chi, N. Huang, C. Lin, R. Li, M.L. Povinelli, P.D. Dapkus, C. Zhou, Toward optimized light utilization in nanowire arrays using scalable nanosphere lithography and selected area growth, *Nano Lett.* 12 (2012) 2839–2845.

[16] Y.T. Lim, J.Y. Son, J.S. Rhee, Vertical ZnO nanorod array as an effective hydrogen gas sensor, *Ceram. Int.* 39 (2013) 887–890.

[17] X. Lu, S. Hoang, W. Tang, S. Du, S. Wang, F. Liu, W. Zhong, S.L. Suib, G. Yang, F.Y. Zhang, P.X. Gao, Direct synthesis of conformal layered protonated titanate nanoarray coatings on various substrate surfaces boosted by low-temperature microwave-assisted hydrothermal synthesis, *ACS Appl. Mater. Interfaces* 10 (2018) 35164–35174.

[18] G. Avgoustopoulos, T. Ioannides, H. Matralis, Influence of the preparation method on the performance of CuO–CeO₂ catalysts for the selective oxidation of CO, *Appl. Catal. B Environ.* 56 (2005) 87–93.

[19] F. Wang, X. Wang, D. Liu, J. Chen, J. Li, Y. Wang, H. Zhang, High-performance ZnCo₂O₄@CeO₂ core@shell microspheres for catalytic CO oxidation, *ACS Appl. Mater. Interfaces* 6 (2014) 22216–22223.

[20] J. Zhang, Y. Cao, C.A. Wang, R. Ran, Design and preparation of MnO₂/CeO₂–MnO₂ double-shelled binary oxide hollow spheres and their application in CO oxidation, *ACS Appl. Mater. Interfaces* 8 (2016) 8670–8677.

[21] S.Y. Chen, W. Tang, J. He, R. Miao, H.J. Lin, W. Song, S. Wang, P.X. Gao, S.L. Suib, Copper manganese oxide enhanced nanoarray-based monolithic catalysts for hydrocarbon oxidation, *J. Mater. Chem. A* 6 (2018) 19047–19057.

[22] Z. Ye, J.M. Giraudon, N. Nuns, P. Simon, N. De Geyter, R. Morent, J.F. Lamonier, Influence of the preparation method on the activity of copper-manganese oxides for toluene total oxidation, *Appl. Catal. B Environ.* 223 (2018) 154–166.

[23] W. Tang, Z. Ren, X. Lu, S. Wang, Y. Guo, S. Hoang, S. Du, P.X. Gao, Scalable integration of highly uniform Mn_xCo_{3-x}O₄ nanosheet array onto ceramic monolithic substrates for low-temperature propane oxidation, *ChemCatChem* 9 (2017) 4112–4119.

[24] S. Todorova, H. Kolev, J.P. Holgado, G. Kadinov, C. Bonev, R. Pereñíguez, A. Caballero, Complete n-hexane oxidation over supported Mn–Co catalysts, *Appl. Catal. B Environ.* 94 (2010) 46–54.

[25] N. Zou, Q. Nie, X. Zhang, G. Zhang, J. Wang, P. Zhang, Electrothermal regeneration by Joule heat effect on carbon cloth based MnO₂ catalyst for long-term formaldehyde removal, *Chem. Eng. J.* 357 (2019) 1–10.

[26] X.-Q. Gong, Z.-P. Liu, R. Raval, P. Hu, A systematic study of CO oxidation on metals and metal oxides: density functional theory calculations, *J. Am. Chem. Soc.* 126 (2004) 8–9.

[27] J. Yuan, W.N. Li, S. Gomez, S.L. Suib, Shape-controlled synthesis of manganese oxide octahedral molecular sieve three-dimensional nanostructures, *J. Am. Chem. Soc.* 127 (2005) 14184–14185.

[28] M.C. Biesinger, B.P. Payne, A.P. Grosvenor, L.W.M. Lau, A.R. Gerson, R.S.C. Smart, Resolving surface chemical states in XPS analysis of first row transition metals, oxides and hydroxides: Cr, Mn, Fe, Co and Ni, *Appl. Surf. Sci.* 257 (2011) 2717–2730.

[29] E.S. Ilton, J.E. Post, P.J. Heaney, F.T. Ling, S.N. Kerisit, XPS determination of Mn oxidation states in Mn (hydr)oxides, *Appl. Surf. Sci.* 366 (2016) 475–485.

[30] J. Jia, P. Zhang, L. Chen, Catalytic decomposition of gaseous ozone over manganese dioxides with different crystal structures, *Appl. Catal. B Environ.* 189 (2016) 210–218.

[31] J. He, Y. Liu, Y. Meng, X. Sun, S. Biswas, M. Shen, Z. Luo, R. Miao, L. Zhang, W.E. Mustain, S.L. Suib, High-rate and long-life of Li-ion batteries using reduced graphene oxide/Co₃O₄ as anode materials, *RSC Adv.* 6 (2016) 24320–24330.

[32] S.L. Suib, Porous manganese oxide octahedral molecular sieves and octahedral layered materials, *Acc. Chem. Res.* 41 (2008) 479–487.

[33] S.Y. Chen, W. Song, H.J. Lin, S. Wang, S. Biswas, M. Mollahosseini, C.H. Kuo, P.X. Gao, S.L. Suib, Manganese oxide nanoarray-based monolithic catalysts: tunable morphology and high efficiency for CO oxidation, *ACS Appl. Mater. Interfaces* 8 (2016) 7834–7842.

[34] H.F. Wang, R. Kavanagh, Y.L. Guo, Y. Guo, G. Lu, P. Hu, Origin of extraordinarily high catalytic activity of Co₃O₄ and its morphological chemistry for CO oxidation at low temperature, *J. Catal.* 296 (2012) 110–119.

[35] W. Liu, M. Flytzani-Stephanopoulos, Transition metal-promoted oxidation catalysis by fluorite oxides: a study of CO oxidation over Cu–CeO₂, *Chem. Eng. J. Biochem. Eng. J.* 64 (1996) 283–294.

[36] S.A. Galema, Microwave chemistry, *Chem. Soc. Rev.* 26 (1997) 233–238.

[37] M. Tsuji, M. Hashimoto, Y. Nishizawa, M. Kubokawa, T. Tsuji, Microwave-assisted synthesis of metallic nanostructures in solution, *Chem. Eur. J.* 11 (2005) 440–452.

[38] G. Chen, Y. Zhao, G. Fu, P.N. Duchesne, L. Gu, Y. Zheng, X. Weng, M. Chen, P. Zhang, C.W. Pao, J.F. Lee, N. Zheng, Interfacial effects in iron-nickel hydroxide–platinum nanoparticles enhance catalytic oxidation, *Science* 344 (2014) 495–499.

[39] A.A. Herzing, C.J. Kiely, A.F. Carley, P. Landon, G.J. Hutchings, Identification of active gold nanoclusters on iron oxide supports for CO oxidation, *Science* 321 (2008) 1331–1335.

[40] W. Tang, M. Yao, Y. Deng, X. Li, N. Han, X. Wu, Y. Chen, Decoration of one-dimensional MnO₂ with Co₃O₄nanoparticles: A heterogeneous interface for remarkably promoting catalytic oxidation activity, *Chem. Eng. J.* 306 (2016) 709–718.

[41] Y. Deng, W. Tang, W. Li, Y. Chen, MnO₂-nanowire@NiO-nanosheet core-shell hybrid nanostructure derived interfacial Effect for promoting catalytic oxidation activity, *Catal. Today* 308 (2018) 58–63.

[42] S. Putla, M.H. Amin, B.M. Reddy, A. Nafady, K.A. Al Farhan, S.K. Bhargava, MnO_x nanoparticle-dispersed CeO₂ nanocubes: a remarkable heteronanostructured system with unusual structural characteristics and superior catalytic performance, *ACS Appl. Mater. Interfaces* 7 (2015) 16525–16535.

[43] X. Xie, Y. Li, Z.Q. Liu, M. Haruta, W. Shen, Low-temperature oxidation of CO catalyzed by Co₃O₄ nanorods, *Nature* 458 (2009) 746–749.

[44] P. Broqvist, I. Panas, H. Persson, A DFT study on CO oxidation over Co₃O₄, *J. Catal.* 210 (2002) 198–206.

[45] J.-Y. Luo, M. Meng, Y.-Q. Zha, L.-H. Guo, Identification of the active sites for CO and C₃H₈ total oxidation over nanostructured CuO–CeO₂ and Co₃O₄–CeO₂ catalysts, *J. Phys. Chem. C* 112 (2008) 8694–8701.

[46] V. Shapovalov, H. Metiu, Catalysis by doped oxides: CO oxidation by Au_xCe_{1-x}O₂, *J. Catal.* 245 (2007) 205–214.

[47] L.R. Merte, G. Peng, R. Bechstein, F. Rieboldt, C.A. Farberow, L.C. Grabow, W. Kudernatsch, S. Wendt, E. Lægsgaard, M. Mavrikakis, F. Besenbacher, Water-mediated proton hopping on an iron oxide surface, *Science* 336 (2012) 889–893.

[48] W. Song, A.S. Poyraz, Y. Meng, Z. Ren, S.Y. Chen, S.L. Suib, Mesoporous Co₃O₄ with controlled porosity: Inverse micelle synthesis and high-performance catalytic Co oxidation at -60°C, *Chem. Mater.* 26 (2014) 4629–4639.